# Corrosion behaviour of biomedical $\beta$-titanium alloys with the surface-modified by chemical etching and electrochemical methods

Cesar Adolfo Escobar Claros, Leonardo Contri Campanelli, Alberto Moreira Jorge, Jean-Claude Leprêtre, Claudemiro Bolfarini, Virginie Roche

▶ **To cite this version:**

Cesar Adolfo Escobar Claros, Leonardo Contri Campanelli, Alberto Moreira Jorge, Jean-Claude Leprêtre, Claudemiro Bolfarini, et al.. Corrosion behaviour of biomedical $\beta$-titanium alloys with the surface-modified by chemical etching and electrochemical methods. Corrosion Science, 2021, 188, pp.109544. 10.1016/j.corsci.2021.109544 . hal-03482636

**HAL Id: hal-03482636**
**https://hal.science/hal-03482636**

Submitted on 24 May 2023

**HAL** is a multi-disciplinary open access archive for the deposit and dissemination of scientific research documents, whether they are published or not. The documents may come from teaching and research institutions in France or abroad, or from public or private research centers.

L'archive ouverte pluridisciplinaire **HAL**, est destinée au dépôt et à la diffusion de documents scientifiques de niveau recherche, publiés ou non, émanant des établissements d'enseignement et de recherche français ou étrangers, des laboratoires publics ou privés.

Distributed under a Creative Commons Attribution - NonCommercial 4.0 International License

Version of Record: https://www.sciencedirect.com/science/article/pii/S0010938X21003103
Manuscript_d61e29a195ad3c21b7019d416c9d3e2e

# Corrosion behaviour of biomedical β-titanium alloys with the surface-modified by chemical etching and electrochemical methods

Cesar Adolfo Escobar Claros [a, b, **], Leonardo Contri Campanelli [b, c], Alberto Moreira Jorge Junior [a, b], Jean-Claude Leprêtre [a], Claudemiro Bolfarini [b], Virginie Roche [a]

[a] Univ. Grenoble Alpes, Univ. Savoie Mont Blanc, CNRS, Grenoble INP*, LEPMI, 38000 Grenoble, France
*Institute of Engineering and Management Univ. Grenoble Alpes
[b] Federal University of Sao Carlos, Graduate Program in Materials Science and Engineering, 13565-905 São Carlos-SP, Brazil
[c] Federal University of São Paulo, Institute of Science and Technology, 12231-280 São José dos Campos-SP, Brazil

**Corresponding author: cesar-adolfo.escobar-claros1@grenoble-inp.fr



© 2021 published by Elsevier. This manuscript is made available under the CC BY NC user license
https://creativecommons.org/licenses/by-nc/4.0/

## Abstract

This work studied the corrosion behaviour of Ti-12Mo-6Zr-2Fe alloy with different surface conditions: untreated and chemically treated (CST), anodised nanotubes (Nt) and nanopores (NP). These samples were immersed in simulated body fluid (SBF) for 1, 7, and 14 days. Samples with Nt and NP displayed higher corrosion resistance and lower passivation current ($i_{pass}$) than untreated and CST samples after 14 days resting in SBF. Furthermore, traditional equivalent circuits and a new two-channel transmission line model were employed to efficiently simulate the electrochemical impedance spectroscopy (EIS) data of the different surface conditions.

**Keywords:** A. Titanium: B. Polarization; B. EIS; C. Anodic films; C. Passive film.

## 1. Introduction

Metallic biomaterials for bone replacement must have four essential characteristics: a) absence of toxic elements thus leading to adequate biocompatibility; b) low stress-shielding effect; c) excellent fatigue performance for cyclically stressed implants, and d) elevated resistance to corrosion [1].

Pure titanium and titanium alloys exhibit desirable characteristics, such as attractive biocompatibility, and adequate corrosion resistance, making them suitable for use in orthopaedic and dental implants. Traditionally, Ti–6Al–4V-ELI (ELI for Extra Low Interstitial content) is used to replace commercially pure titanium in biomedical applications [2]; however, this alloy can fail indirectly due to stress

shielding and present toxic reaction with the human body [3,4].In this context, new alloys with non-toxic elements and lower elastic modulus have been developed, such as the commercial β Ti-12Mo-6Zr-2Fe alloy (TMZF) with high mechanical strength and moderate-low elastic modulus [5].

Despite the metallurgical and mechanical features, surface treatments are essential to enhance the osteointegration process of titanium alloys. Previous studies have demonstrated that HCl etching plus NaOH treatment can be an effective way to develop nanometric topographies on the Ti–6Al–4V surface, keeping its static and cyclic mechanical properties [6]. An alternative to CST is the anodisation process. Anodisation is widely used on pure titanium to create $TiO_2$ nanotube layers with nanometric topography that maximises the surface area, thus leading to better bioactivity [7–10].

Corrosion of metallic prosthesis is known to modify their structural integrity and cause alterations of the surrounding environment, such as changes in pH and decrease of dissolved oxygen. Furthermore, the metal ions released may cause an allergic response and be harmful to the patient [11–13]. For these reasons, the study of corrosion properties is critical and necessary for metallic biomaterials.

In recent years, the Electrochemical Impedance Spectroscopy (EIS) has been successfully applied to polarization resistance measurement and determination of corrosion mechanisms in different systems [14,15]. Through EIS, it is possible to obtain information concerning to electrochemical properties of electrolyte and electrode. Additionally, this technique can discriminate several reactions on the electrode surface.[16,17].

Oxide and porous passive layers show complex impedance responses, and the understanding of their impedance behaviour is not straightforward. Recently, different titanium electrodes were studied through impedance using non-traditional models termed transmission line models (TLM), showing excellent consistency between experimental and modelled results, and obtained parameters with excellent reliability [18–20].

Therefore, this work aimed at a throughout corrosion study of TMZF surfaces treated by CST, Nt, and NP and compared to untreated ones. Such a study was performed in samples immersed by different periods in SBF, which were analysed by potentiodynamic polarization and electrochemical impedance measurements.

## 2. Materials and methods

The commercial β TMZF alloy produced by ERCATA GmbH was used in this study. TMZF bars were cut into disks of 10 mm diameter and 1 mm thick, heat-treated at 800 °C for two hours, and then water quenched to obtain a fully recrystallised beta phase structure [5].

### *2.1 Surface modification processes*

Four different surface conditions were developed on TMZF samples: untreated surface, surface treated with HCl etching and alkaline NaOH solution (CST), and two anodised condition – nanotubes (Nt) and nanopores (NP).

Before surface modifications, TMZF disks were sequentially ground by SiC emery papers using the grades P240, P320, P600, P1200, and P2400. After which, they were conventionally polished using 3 and 1 μm alumina. Deionised water

(Milli-Q®), ethanol, and acetone were used to clean the finished surfaces. Such surface condition was named untreated surface.

For the CST, the grounded samples were immersed into an HCl (37 wt.%) solution heated at 60 °C for 30 min. Samples were individually alkali-treated in 45 ml NaOH 10 mol•$L^{-1}$ contained in polyethylene receptacles. The alkaline solution was maintained at 60 °C for 24 h. The disks were soaked into deionised water and sonicated for 10 min, followed by 10 min in acetone.

The anodisation processes were carried out in an electrochemical cell with a conventional two-electrode arrangement. The counter electrode (cathode) was a cylindrical platinum grid placed ~3 cm away from the polished disks, which were used as the working electrode (anode). The anodisation processes were performed at 25 °C in an organic electrolyte consisting of glycerol, containing 25 vol% of water and 0.25 M of $NH_4F$. The DC constant potential applied to produce Nt and NP were 10 V during 2 h, and 20 V during 1 h, respectively. Amorphous as-anodised surfaces were heat-treated in the air at 550 ºC for 2 h, thus crystallising the amorphous $TiO_2$ nanostructured surfaces into a rutile/anatase phase mixture [18].

The surfaces were inspected in a Zeiss Ultra-55 FEG scanning electron microscope (SEM). InLens detectors were used to acquire high spatial resolution images. For such, beam energy of 10 keV and a work distance of ~6 mm was employed. Additionally, chemical analyses of the different surface treatments were performed by an X-ray photoelectron spectroscopy (XPS). A Vacuum Generator XR3E2 apparatus with an Mg-Kα X-ray source (characteristic energy hv = 1273.6 V) at 15 kV and 20 mA operating conditions was used to perform the XPS

measurement. The binding energies were also calibrated by the C1s hydrocarbon peak at about 285 eV through the Advantage software package, and the peaks were fitted using smart baseline subtraction.

### *2.2 Electrochemical characterisation*

The electrochemical characterisation was carried out in a potentiostat (Gamry Instruments, Reference 600+), employing 250 ml of SBF solution at 37 °C and pH 7.40. This solution was prepared according to the ISO 23317 specification and employing analytical grade reagents NaCl (8.035 $g.L^{-1}$), $NaHCO_3$ (0.355 $g.L^{-1}$), KCl (0.225 $g.L^{-1}$), $K_2HPO_4.3H_2O$ (0.231 $g.L^{-1}$), $MgCl_2.6H_2O$ (0.311 $g.L^{-1}$), $CaCl_2$ (0.292 $g.L^{-1}$), $Na_2SO_4$ (0.072 $g.L^{-1}$) and deionised water. A standard three-electrode cell was utilised, where the working electrode was the surface of TMZF samples, where an area of 0.283 $cm^2$ was exposed. A flat platinum mesh and a Saturated Calomel Electrode (SCE, 0.242 V vs SHE, at 25 ºC) were, respectively, the counter and reference electrodes. A distance of ~3 cm was invariably held between the counter and working electrodes. The SCE electrode, which was positioned near the working surface, was electrically associated in parallel to a platinum wire connected to a capacitor of 1 µF to avoid capacitive and inductive artefacts that may happen during high-frequency impedance measurements [21].

The experimental assembly was placed inside a Faraday box cage connected to the ground. It reduces current noise picked up by the working electrode and voltage noise caught by the reference electrode. Additionally, the electrochemical characterisations were executed in a dark environment, thus reproducing physiological conditions [22].

Firstly, the characterisation sequence consisted of recording the Open Circuit Potential (OCP) evolution during 1 hour of soaking into the SBF until reaching the stable state. Subsequently, electrochemical impedance spectroscopy (EIS) was performed at the OCP. The system was perturbed by a sine-wave whose amplitude was 10 $mV_{rms}$ vs OCP within the range of frequencies of $10^{-2}$ to $10^{4}$ Hz. The amplitude was large enough for both the easiness measurement of the output signal and satisfying the linearity criterion. Finally, the resistance to corrosion was assessed through potentiodynamic polarization curves recorded over the potential range of -0.03 V/SCE to +1.2 V/SCE relative to the OCP, with a scan rate of 0.3 $mVs^{-1}$. These corrosion tests were performed over untreated samples, CST, Nt, and NP in four different immersion periods inside the SBF solution: 0, 1, 7, and 14 days. Three samples were evaluated per condition and soaking time (different samples each time, but with the same surface treatment).

The program used to adjustment and simulate impedance parameters was the SIMAD® software. It was developed at the Laboratoire Interfaces et Systèmes Electrochimiques (LISE) at Pierre et Marie Curie University (UPMC) [23].

## 3. Results and discussion

Fig. 1 shows high-resolution SEM images of the four different surface conditions studied. Fig. 1a shows the as-polished untreated TMZF sample surface, which will be used as the reference state during the different electrochemical tests. Fig. 1b presents the sample surface after CST treatment where one may observe the etching effect on changing the initial smooth morphology to a microporous surface or coral-like structure in the submicrometric and nanometric scale. Fig. 1c

shows the anodised Nt samples exhibiting a network of vertically self-organised nanotubes uniformly distributed over the entire TMZF surface, and Fig. 1d shows the anodised NP surface, characterised by a nanometric and disordered worm-like structure.

The surface characterisation technique XPS was applied to evaluate the detail chemical bonds formed over the untreated and treated TMZF sample before the immersion periods and the electrochemical tests. High-resolution spectra were shown in Fig. 2 a–d. The standard binding energies were determined according to the standard elements from the NIST XPS database [24]. The untreated sample displayed strong Ti-2p, Mo-3d, Zr-3d, and O-1s peaks. The Ti-2p spectrum (Fig. 2a) can be fitted into $Ti^{4+}$ (458.48 eV and 464.28 eV), $Ti^{3+}$ (458.08 eV and 463.28 eV), and $Ti^{0}$ (454.22 eV and 460.62 eV), which corresponded to $TiO_2$, $Ti_2O_3$ and metallic titanium, respectively. Similarly, the Mo-3d spectrum was fitted into $Mo^{+4}$ (229.57 eV and 232.90 eV) and $Mo^{+6}$ (231.93 eV and 235.27 eV) corresponding to $MoO_2$ and $MoO_3$, respectively. The O-1s spectrum can be divided into three peaks, $O^{2-}$ (529.90 eV), the peak relates to -OH (530.57 eV), and the oxygen bound in the absorbed $H_2O$ (532.23 eV). The Zr-3d spectrum was fitted into $Zr^{4+}$ (182.13 eV and 184.51 eV), referring to $ZrO_2$. Similar analyses were conducted over CST samples (Fig. 2b); in this surface condition was not observed the $Ti^{0}$ peaks, due to the formation of the sodium titanate layer on the sample surface, as observed in Fig. 1b. As shown in the Na-1s spectrum from Fig. 2b, the binding energy at 1071.53 eV is characteristic for Na-1s and assigned to the Na–O bond of sodium titanates [25]. Distinctive peaks from molybdenum oxides were not observed in the CST samples,

and the peaks related to zirconium oxides showed low intensity. Both anodised conditions, Nt, and NP show similar spectra (Fig. 2c and 2d, respectively); here, the high-resolution spectra of Ti-2p show as expected only the contribution of the Ti-2p3/2 and Ti-2p1/2, characteristic for $Ti^{4+}$ state of $TiO_2$ [26]. The Mo-3d spectra from Fig 2c and 2d show the presence of the MoO3 and a non-stoichiometric oxide $MoO_x$ [27], indicating that the anodisation process promotes the transformation of the naturally formed $MoO_2$ to the MoO3 and $MoO_x$ [28].

The XPS spectra (Fig. 2) show the chemical differences among the different surface condition. On the untreated samples was detected the presence of $TiO_2$, $Ti_2O_3$ and metallic titanium. As expected, the CST surface is mainly composed of sodium titanate. Furthermore, the anodisation process and the subsequent thermal treatment favoured the surface transformation to more stable titanium oxide ($TiO_2$). We calculated the Ti/Mo oxides ratio and observed an increase from the value of the untreated condition (0.07) to 0.39 for Nt and 0.32 for NP. These surface characteristics help to create a more corrosion resistant surface [29], as observed in Fig. 9.

Fig. 3 compares the typical potentiodynamic polarization curves of a representative sample for each surface condition and immersion time. From these curves, it was calculated the corrosion potential ($E_{corr}$) corresponding to the position where the net current is zero and is indicated as the "peak" directed downwards on the polarization curves.

The inherent features of the polarization curves indicated a stable passive behaviour for all surface conditions and immersion periods. However, after 0 days,

samples covered by nanotubes produced curves with fluctuations in the passive domain because of the creation of a localised aggressive environment that breaks the passivation layer [11]. These kinds of oscillations can be attributed to the competition between the passive-film establishment and dissolution. Remained fluoride ions trapped into the tubes from the anodisation process could enhance this phenomenon [30].

The values of $E_{corr}$ for the four different surface treatments are summarised in Fig. 4. Such open circuit potential values are comparable to those obtained for each condition after immersion for one hour. Initially, untreated samples show a low corrosion potential close to -0.370 $V_{SCE}$. However, this value increases considerably after one day of immersion and remains almost constant at -0.050 $V_{SCE}$ until 14 days in the SBF solution.

Furthermore, CST, Nt, and NP samples showed a nobler behaviour (-0.190, -0.072, and -0.115 $V_{SCE}$, respectively) compared to untreated samples without previous immersion (0D). This behaviour was less pronounced for samples treated with HCl plus NaOH, indicating a lower corrosion resistance than samples after anodisation (Fig. 4). After soaking in SBF for one day, all of them tended to higher potential values close to -0.050 $V_{SCE}$.

As part of this study, rather than corrosion current density ($i_{corr}$), the current density of the passivation plateau ($i_{pass}$) was chosen to establish a better comparison between the different surfaces obtained, which are likely to passivation. However, in some passivated materials exposed to physiological environments, the current density is not independent of the potential in the passive state. One reason is the

dynamic character of the test, i.e., the changes of the passive film with the applied potential are prolonged to remain stable with the scan. Another possibility may be that changes in the passive layer are uncompensated for the increased oxidative driving force during the measurement [11].

In practice, the shapes of branches anodic are not identical for all the samples (Fig. 3), and the determination of $i_{pass}$ may not be straightforward. Thus, the sample $i_{pass}$ was obtained from the average of current densities measured in the potential range of +0.4 $V_{SCE}$ and +1 $V_{SCE}$ relative to the OCP [7].

Fig. 5 presents values of $i_{pass}$ and the category of the resistance to corrosion of the different surface treatments in different immersion times. Untreated specimens show moderate-to-low and long-lasting results with $i_{pass}$ closer to 2.0 $\mu A.cm^{-2}$ during the different periods analysed, because of the existence of a homogenous and thin passive layer on the alloy surface.

From an electrochemical standpoint, samples with CST showed the lower corrosion resistance among the four systems for the various immersion times, showing $i_{pass}$ values higher than 12 $\mu A.cm^{-2}$ for 0, 1, and 7 days soaking in SBF. However, after 14 days, it was possible to see a reduction in its $i_{pass}$ value (~8.0 $\mu A.cm^{-2}$). This chemical treatment produces micro, submicron, and nanometre features on the titanium sample. These fine network structures are favourable to accelerate hydroxyapatite nucleation because of the development of a sponge-like structure. However, this structure facilitates the diffusion and charge transfer amid electrolyte and the TMZF substrate [31].

Initially, for 0 and 1 day of immersion, Nt samples showed high $i_{pass}$ values of around 5.0 μA.cm$^{-2}$. Nonetheless, after 7 and 14 days, the $i_{pass}$ values were lower than 0.8 μA.cm$^{-2}$. In the beginning, ordered nanotubes offered free paths for ion diffusion between the electrode and the bulk electrolyte. After a few immersion days, these channels began to close by the deposition of calcium phosphate on the outer and bottom nanotubes parts, with additional growth of the inner passive film [32], which could have hindered the transfer of ions through such channels.

NP samples exhibited good electrochemical behaviour with low and stable $i_{pass}$ values during all immersion periods, exhibiting $i_{pass}$ values smaller than 0.3 μA.cm$^{-2}$ after 14 days soaked in SBF. This performance was correlated with the homogeneous passive layer formed on the TMZF surface, which is thicker than the passive layer of the untreated samples.

Additional electrochemical information is obtained from EIS measurements and respective data elucidation. Fig. 6 presents the evolution of Nyquist plots and Bode diagrams with immersion times in SBF of untreated TMZF samples (polished surfaces); replicate specimens showed similar results but were not plotted for better visualization of the diagrams (reproducibility was checked). Bode representations were rectified for the ohmic resistance (resistance of the electrolyte ($R_e$)), roughly calculated between 20-30 Ω.cm$^2$, which was deduced from the frequency of $f = 10^4$ Hz (high-frequency limit).

Fig. 6a presents the Nyquist diagram for untreated samples, which reflects the typical response of a capacitive-resistive or pseudocapacitive system independent on the immersion time. It signifies that the charge transfer, and therefore the

reactions are limited because of the protective behaviour of the passive oxide layer [22,33].

The continuous increase of the impedance modulus |Z| throughout the immersion time suggests that the first two weeks in SBF enhances the resistance to corrosion of untreated samples (Fig. 6d). This observation is consistent with the $E_{corr}$ measurements (Fig. 4), which shows a significant increase from the first day of immersion and remains almost constant until 14 days.

Bode plot has been useful in recognising the number of time constants of a system checking the validity of an Electrical equivalent circuit (EEC). These curves are more sensitive to modelling parameters than other traditional impedance plots. Nevertheless, the presence of the ohmic resistance (electrolyte resistance) covers up the real behaviour at high frequencies. For this reason, modified Bode curves corrected from ohmic resistance are used as a reliable option when the solution resistance is not negligible [34]. Therefore, all Bode diagrams in this work were corrected from the resistance of the electrolyte using Eqs. 1 and 2.

The impedance modulus was corrected according to:

$$|Z|_{corrected} = \sqrt{(Z_r - R_e)^2 + {Z_i}^2} \quad (1)$$

The phase angle can be obtained from:

$$\Phi_{corrected} = tan^{-1}\left(\frac{Z_i}{Z_r - R_e}\right) \quad (2)$$

where |Z| is the impedance modulus, $\Phi$ the phase angle, and $Z_r$ and $Z_i$ the impedance real and imaginary parts, respectively.

Over the untreated TMZF samples, it is expected the formation of a passive bi-layer, which has been observed in similar titanium alloys containing zirconium and molybdenum [35]. This passive bi-layer would be composed of an external porous layer and an inner barrier layer; thus, it is expected to find two relaxation processes or time constants from the impedance results.

The main disadvantage of the corrected Bode phase plot is the need for a precise assessment of the electrolyte resistance. Inaccurate estimations could provide the wrong idea of an additional time constant at high frequencies. Besides that, the corrected curves are very susceptible to data noise at high frequencies [36]. For these reasons, a complementary curve for the corrected Bode plots is the graphical description of the effective CPE exponent ($\alpha_{eff}$), extracted from the impedance imaginary part ($Z_i$) according to [36]:

$$\alpha_{eff}(f) = \left| \frac{d\log |Z_i(f)|}{d\log f} \right| \quad (3)$$

Traditionally, in the curve of $\alpha_{eff}$, the constant phase elements (CPE) are correlated with plateaus extended during various levels of frequencies. However, these regions can decrease to form bumps or smooth peaks because of the interaction of events with close relaxation processes [36]. Therefore, Figs. 5b and c clearly show two-time constants for all samples, and thus modelled by two CPE, one of them ranging from $10^{-2}$ Hz to $10^{2}$ Hz and the second one in high frequency (around $10^{4}$ Hz). Thus, using the corrected-Bode phase plot and the graphical illustration of the $\alpha_{eff}$, it was proposed an EEC for modelling the impedance results obtained from the untreated samples (Fig. 6a).

In the electrical circuit of Fig. 6a, $R_e$ denotes the SBF solution resistance. The suffix B and OP are correlated with the elements that represent the inner barrier layer and the outer porous oxide layer, respectively. Here, instead of using a pure capacitor, CPE was used because of the assumption of heterogeneous charge distribution on samples surfaces [35,37].

A phase element impedance is defined as $Z_{CPE} = [Q(j\omega)^{\alpha}]^{-1}$. The α value is associated with the heterogeneous distribution of current as a result of the non-uniform surface. The capacitance is *Q*, while *j* and *ω* are the current and frequency, respectively. The values of resistance, capacitance, and α for porous and barrier layers, obtained by adjusting the experimental data using the EEC, are given in Table 1. The α values close to 0.9 suggest that the behaviour of such passive layer approaches that of an ideal capacitor, immersion time-independent [37].

The similarity between experimental and simulated results denote that the proposed equivalent circuit fits well the experimental data. Error-values (*X*) lower than 1% were found during the EIS data treatments, indicating a satisfactory fitting level (Table 1) [18].

The resistance values, $R_B$, related to inner barrier layers, increase with the immersion days and are significantly larger than the values related to outer porous layers, $R_{OP,}$ which remain nearly constant, as Table 1 shows. These results show that the protection provided by the passive layer is predominantly because of the inner barrier layer, as also observed in other titanium alloys [35,38,39].

From the values of CPE (Q and α), $R_e$, and $R_{OP}$, $R_B$ and using the Brug equation (Eq. 4), one may obtain the effective capacitance for the passive layer, considering the titanium surface composed of an outer porous layer and a compact inner layer.

$$C_{eff} = Q^{1/\alpha}({R_e}^{-1} + {R_{OP,B}}^{-1})^{(\alpha-1)/\alpha} \qquad (4)$$

The $C_{eff}$ calculated from the values listed in Table 1 for the diverse immersion periods ranged from 18 to 9 μF.cm$^{-2}$ for the porous layer and 12 to 3 μF.cm$^{-2}$ for the compact inner layer, values similar to the ones observed for AISI 316L stainless steel immersed in physiological solutions [40,41]. This capacitance reduction is related to a passive layer thickness increase [18,42]. Traditionally, low capacitance values are linked with nobler electrochemical behaviour [39,42].

The calculation of the thickness of the compact inner layer passive film can be made using Eq. 5, which is valid for the parallel-plate capacitor model of a homogeneous oxide layer, associating the overall effective capacitance to the protective oxide layer:

$$d_{ox} = \frac{\varepsilon_r \varepsilon_0}{C_{ox}} \qquad (5)$$

Where $\varepsilon_0$ is the vacuum permittivity (8.85x10$^{-14}$ F.cm$^{-1}$), and $\varepsilon_r$ is the material relative dielectric constant (taken as $\varepsilon_r$ = 100, the dielectric constant of $TiO_2$ [18]). By using this information, it was possible to obtain an approximation of the passive layer thickness for the diverse immersion days. The passive layer grew with the increase of the immersion days, initially, with 7 nm for non-immersed samples, to 27 nm after 14 days (Fig. 7).

Fig. 8 presents the impedance curves for the acid and alkali-treated samples. The impedance results in the Nyquist plots displays semicircles arc flattened at low frequencies. The radius of these arcs decreases with the increase of immersion time (Fig. 8a).

Figs. 8b and d show the Bode curves of CST samples soaked in SBF for different immersion times. Samples without previous immersion exhibit a progressive increase of the phase angle from high to middle frequencies, with a variation of the phase angle from -54° to -27°. After that, the phase achieved a minimum value of -74° in the frequencies between $10^0$ Hz – $10^1$ Hz and remained approximately constant. This behaviour could be related to the sodium titanate layer formed on the substrate during the CST (see Table S1 in the supplementary material); this layer is considered low capacitive because of its porous nature.

A uniform variation in the phase angle curves is observed with the increase of immersion periods. At intermediate frequencies, a slight reduction in the phase angle was observed in samples immersed for 1 and 7 days compared to samples without previous immersion. This behaviour was related to the precipitation and growth of the first nucleus of calcium phosphate on the sample surface (Fig. 9a and Fig. S1 of the supplementary material). In the same region, after 14 days of immersion, the plateau appeared in a higher phase angle (around -62°) because of the presence of a highly dense calcium phosphate layer (Fig. 9b).

As it was shown in Fig. 6d, untreated samples exhibited a performance similar to a blocking electrode characterised by a slope value of -1 at all frequencies. However, irrespective of the immersion period, the CST samples behave differently

and show plots with slopes below one at the lower frequency region (Fig. 8d), indicating a typical behaviour of a more reactive electrode [37].

The effective CPE exponent ($\alpha_{eff}$) plot is used to characterise better the relaxation process occurring over the surface of chemically treated samples. Fig. 8c shows similar behaviour at high and intermediated frequencies to the corrected-phase plot. Nevertheless, this plot shows an additional bump at low frequencies ($10^{-2}$ Hz to $10^{-1}$ Hz). This exciting behaviour was ascribed to an extra relaxation process.

Over the CST three relaxation processes are expected to act during the impedance test, one above the two found in the untreated samples, which is related to the external sodium titanate layer created during the chemical treatment with HCl and NaOH. Fig. 8a presents the EEC, which provides a good representation for systems with a compact inner layer, an intermediate porous oxide layer, and an outer gel sodium titanate layer.

In the EEC (Fig. 8a), $R_e$ represents the resistance of the electrolyte, $R_{OP}$ and $CPE_{OP}$ represent the resistances and the capacitances of the outer porous layer, related with the dissolution of the gel sodium titanate layer and the HAp growth (see Table S1 in the supplementary information file). $R_{IP}$ and $R_B$ are the resistances of the intermediate porous oxide layer and the inner barrier layers, and the $CPE_{IP}$ and $CPE_B$ are used to designate the capacitances of the outer porous layer and the compact inner layer, respectively.

The Nyquist plots of the EIS data of CST samples were modelled through the EEC shown in Fig. 8a. The errors measured ($X$) for the experimental and simulated

data were lower than 1% independently of the immersion period, indicating a satisfactory fitting level. The parameters of the electrochemical impedance such as resistance, capacitance, and α values, regarding the porous and barrier layers obtained from the equivalent circuit, are presented in Table 2.

With the increase from 0 to 7 immersion days, the $Q_{OP}$ values decreased, showing a dissolution process of the gel sodium titanate layer. This behaviour might be related to the interaction between ions present in the physiological solution and ions in the titanate layer [32]. Between 7 and 14 days in the SBF, a mature HAp layer arose from the complete dissolution of the sodium titanate layer as can be seen in Fig. S1 of the supplemental material, which acts as a diffusion barrier corroborated by the higher $\alpha_{OP}$ value at 14 days. This behaviour is confirmed in the Nyquist spectrum at 14 days of immersion (Fig. 8a), where it is possible to see a semicircle arc smoothed at low frequencies [32].

The resistance $R_B$ decreased continuously, and concomitantly, the $R_{OP}$ increased with the immersion days, attaining a constant value between 7 and 14 days. This behaviour can be linked with the continuous dissolution and formation processes of the barrier layer and the HAp layer, respectively [32].

Previous investigations employing Auger emission spectroscopy confirmed the presence of an oxide film between the sodium titanate layer and the titanium surface [43,44]. Through the impedance results and employing the Eq. 5 and the fitted results $C_{effB}$ from Table 2, it is possible to calculate an approximate value of the titanium oxide inner layer thickness, whose values are summarised in Fig. 7b.

CST samples without immersion in SBF showed a thinner compact layer compared with the untreated samples in the same condition. During acid etching with HCl, the thin passive titanium oxide layer dissolves to form $TiH_2$; immediately after, in contact with air moisture, a new titanium oxide film is developed. However, this layer is thinner than the initial one [45–47]. Similar to the untreated samples, the passive layer on the CST samples grew with the increase of the immersion days (Fig. 7b).

The Nyquist diagrams observation reveals that regardless of the immersion time studied, the nature of the CST impedance spectra (arcs) is typical of a reactive system. In contrast, in Fig. 10a the samples with Nt are apparently rather purely capacitive (straight line), or leastwise pseudocapacitive (inclined straight line), indicating that the faradaic reactions are very limited [37].

The corrected Bode phase angle plots of TMZF samples with Nt immersed in SBF are presented in Fig. 10b. At low and middle frequencies ($10^{-2}$ Hz to $10^{1}$ Hz), the phase angle remains almost constant with values approaching -90°, which is the typical capacitive behaviour of a compact oxide film. The protective character of this film seemed to be enhanced with increased immersion, indicating a more protective behaviour after 14 days.

Fig. 11 presents Nyquist plots and the Bode diagrams evolutions with the immersion time in the SBF solution, for the TMZF samples with NP. Similarly, to Nt, NP specimens show a capacitive or pseudocapacitive behaviour, which was observed in the Nyquist diagram independently of the immersion time studied (Fig. 11a).

The plots of impedance modulus of TMZF samples anodised with NP showed a stable behaviour, characterised by two distinct zones (Fig. 11d). Between low and middle-frequency ($10^{-2}$ Hz – $10^{1}$ Hz), the curves exhibited a constant linear slope close -1, less inclined than the slope at higher-frequencies, around to -0.5. Similar behaviour was observed in Nt samples in Fig. 10d, which is characteristic of capacitive surfaces [30].

Given the information obtained through the Bode phase and the $\alpha_{eff}$ plots (Fig. 10c and Fig. 11c), initially, both anodised conditions, Nt, and NP were fitted considering a similar electrical circuit as the one used for untreated samples (two-times constant). However, the fitting results for both anodised conditions were not satisfactory, as already mentioned in other works [18]; the adjustment errors are large, and the values of the parameters obtained are outliers.

An alternative model was proposed by R. De Levie and then by Bisquert to interpret the physical and chemical phenomena in porous electrodes, denominated Transmission Line Model (TLM) [48,49]. Recently titanium electrodes have been studied through impedance using TLM. These studies have shown excellent compatibility between experimental and modelling results, consistency in the parameters obtained, and a more precise interpretation of the impedance results obtained through EIS tests [19,20,22]. Thereby, a TLM was employed to simulate the impedance response of Nt and NP samples in SBF.

Fig.12 shows the TLM proposed in this work; employing it for modelling various microstructures and geometries regarding different hypotheses. Additionally, it is essential to stress that this model involves the volume processes distributed over

the whole electrode surface. Channel 1 is represented as a distributed resistance ($R_1$), and the transport behaviour in channel 2 by a parallel arrangement of a resistance ($R_2$) and a CPE element ($Q_2$). The interfacial pseudocapacitance is represented by $Q_3$ and the endpoints parameters by the resistance and capacitance, $R_A$, and $Q_B$, respectively.

The TLM is composed of ten parameters that satisfactorily describe the interface behaviour (these parameters are explained in detail in the supplementary material and elsewhere [18,49,50]). The error between the experimental points and the simulation was lower than 1.0 %, independent of anodised morphology and immersion time. Only the nanotube condition after 14 days showed a higher value (1.7%), which is quite reasonable.

Traditionally, during the EIS measurements, the crossover frequency ($\omega_c$) is higher than the highest frequency level analysed, and for this reason, the material generally behaves like a purely resistive component. However, low conductive materials show low $\omega_c$ values [50], and thus, is then expected that in this study the $\omega_c$ be lower than the range of frequencies employed during the impedance test. Therefore, the oxide channel will display anomalous transport behaviour.

Table 3 shows the electrochemical impedance parameters obtained by adjusting the experimental results of Nt samples for the diverse immersion days. Additionally, the $\omega_c$ values representing the transport mechanism through the channel 2 ($X_2$) were calculated using Eq. 6.

$$\omega_c = \frac{1}{r_2\, q_2\, (iw)^{1/\beta}} \qquad (6)$$

The pseudocapacitance values $Q_3$ varies as the immersion time increases; this could indicate the processes of formation and dissolution of small nuclei of calcium phosphates on the nanotubes' walls. Between days 7 and 14, the nucleation process is favoured, showing an evident decrease in the interface impedance. Besides, the coefficient b is close to 1, showing homogeneity and stability of the pore walls, independently of the immersion time.

Fig. 13 presents the behaviour of the endpoints $Z_A$ and $Z_B$ during the immersion days, represented by resistance and capacitance of $R_A$ and $Q_B$, respectively.

During the immersion time in SBF, the resistance $R_A$ gradually increases, and the $Q_B$ decreases. This behaviour could be related to the development and growth of calcium phosphate nuclei (Initial step to the apatite formation) on the outer part of the nanotube and the bottom part of the channel. This behaviour is observed in Fig. 14 (red circles). Additionally, the $Q_B$ decrease could be related to the growth of the inner passive film [32].

Table 4 shows the electrochemical impedance parameters obtained by adjusting the experimental results of NP samples for the diverse immersion days. For the Nt and NP fitting analysis, the average channel length (L) was $2x10^{-5}$ cm.

For NP samples, the pseudocapacitance $Q_3$ values are lower compared to Nt and remain almost constant regardless of the immersion time, because of the stable behaviour of the interfacial impedance ($\zeta$), even in the first immersion days. Besides, the coefficient b is close to one showing homogeneity and stability of the pore walls.

Fig. 15 presents the endpoints parameters represented by the resistance and capacitance, $R_A$, and $Q_B$, respectively. These values were graphed to understand the behaviour of the transmission line endpoints ($Z_A$ and $Z_B$) during the immersion days of the NP samples. The values of $R_A$ and $Q_B$ were obtained from Table 4.

During the immersion time in SBF, the resistance $R_A$ gradually increases. This behaviour could be ascribed to possible nucleation and growth of hydrated silica gel and amorphous calcium phosphate on the outer and inner parts of the nanopores, both predecessors for the apatite formation [51] (see Fig. S1, supplemental material). This behaviour could be observed in Fig. 1 (red circles). Moreover, the $Q_B$ values were low and constant, indicating a stable and protective behaviour of the inner passive film during the entire time analysed.

As it was indicated, the transport behaviour in channel 2 ($X_2$) is defined by a different model termed as "anomalous transport model" (a CPE, $Q_2$, and a resistance, $R_2$, parallelly connected), because the charge carrier transport mechanism is frequency-dependent (Eq. S3). For both anodising conditions, Nt, and NP, $\omega_c$ was between 0.003 to 0.035 Hz (Eq. 6). These low values indicated a low charge transfer through the channel 2 in the frequency regime studied in this work ($10^{-2}$ - $10^4$ Hz).

Fig. 17 summarises the corrosion response after 14 days of soaking in SBF of the diverse surface conditions studied in this work; comparing the barrier resistance values ($R_B$ for untreated and CST samples or $R_A$ for the anodised samples) related with the resistance to corrosion obtained from the impedance data, and the $i_{pass}$ obtained from the polarization curve.

Untreated samples showed a good corrosion response indicated by a high resistance value and acceptable $i_{pass}$, lower than 2 μA.cm$^{-2}$. Samples treated with HCl and NaOH, contrary to untreated samples, showed a low corrosion resistance proved by the lowest $R_B$ and the highest $i_{pass}$ values. Finally, the anodised samples showed the best corrosion resistance corroborated by the highest and lowest values of $R_A$ and $i_{pass}$, respectively.

## 4. Conclusion

The electrochemical behaviour of the four different treated surface samples has been successfully studied, and the conclusions are summarised in the following paragraphs:

- $E_{corr}$ values revealed that Nt and NP surfaces showed a nobler behaviour than the untreated and CST ones, indicating a more protective surface. Moreover, although these anodised surfaces showed moderate $i_{pass}$ values in the early stages of immersion (0 and 1 day), after 14 days immersed in SBF, they showed the lowest values, close to 0.2 μA.cm$^{-2}$.
- Nyquist and Bode plots for the untreated TMZF samples showed a pseudocapacitive behaviour due to their very protective passive layer. The continuous increase of the impedance modulus in these samples suggested that the resistance to corrosion enhances with the immersion time.
- Through the Nyquist and Bode curves, the CST samples showed a more reactive behaviour compared with the untreated samples, independently of the immersion time in SBF. In these samples, after 14 days of immersion, it was

possible to observe variation in the impedance curve, which was associated with the formation of the HAp layer over the surface.

- Together with the objective of forming a thicker and denser oxide layer by the anodizing process, the increased presence of $TiO_2$ and molybdenum oxides helped create a more protective surface against corrosion.
- Impedance curves of the anodised samples in SBF revealed a capacitive or at least pseudocapacitive behaviour, corroborating the protective response of these surface conditions. Additionally, it was observed a particular behaviour that could not be modelled by the traditional equivalent circuits. Thus, it was proposed a two-channel transmission line model for analysing the impedance results successfully.

**Acknowledgements**

The authors are grateful to the French Committee for the Evaluation of Academic and Scientific Cooperation with Brazil (COFECUB) and the Brazilian Coordenação de Aperfeiçoamento de Pessoal de Nível Superior - Brazil (CAPES) for funding the bilateral cooperation under the grant #88887.137755/2017–00. This study was financed in part by the Coordenação de Aperfeiçoamento de Pessoal de Nível Superior – Brasil (CAPES) – Finance Code 001. CAEC and LCC thanks CNPq (Brazil) under the grant #141952/2019-9 and #150782/2019-5. The authors acknowledge CNPq (Brazil) under the grants universal project #403955/2016-5 and 409847/2016-0. AMJJ would like to acknowledge the CNPq (Brazil) under grant #301429/2017-0.

## Data availability

The raw/processed data that required to reproduce these findings cannot be shared at this time due to technical or time limitations.

## References


[1] S. Minagar, C.C. Berndt, J. Wang, E. Ivanova, C. Wen, A review of the application of anodization for the fabrication of nanotubes on metal implant surfaces, Acta Biomater. 8 (2012) 2875–2888. https://doi.org/10.1016/j.actbio.2012.04.005.

[2] C.N. Elias, J.H.C. Lima, R. Valiev, M.A. Meyers, Biomedical applications of titanium and its alloys, J. Miner. Met. Mater. Soc. 60 (2008) 46–49. https://doi.org/10.1007/s11837-008-0031-1.

[3] Australian Orthopaedic Association National Joint Replacement Registry (AOANJRR). Hip, knee & shoulder arthroplasty - Annual Report 2018, Adelaide AOA, 2018. (2018) 1–444. www.aoa.org.au.

[4] A. Ito, Y. Okazaki, T. Tateishi, Y. Ito, In vitro biocompabitibility, mechanical properties, and corrosion resistance of Ti-Zr-Nb-Ta-Pd and Ti-Sn-Nb-Ta-Pd alloys, J. Biomed. Mater. Res. 29 (1995) 893–900.

[5] ASTM F1813-13, Standard Specification for Wrought Titanium-12Molybdenum-6Zirconium-2Iron Alloy for Surgical Implant, ASTM Int. (2013) 1–5. https://doi.org/10.1520/F1813-13.2.

[6] C.A.E. Claros, D.P. de Oliveira, Fatigue behavior of Ti–6Al–4V alloy in saline solution with the surface modified at a micro- and nanoscale by chemical

treatment, Mater. Sci. Eng. C. 67 (2016) 425–432. https://doi.org/10.1016/j.msec.2016.04.099.

[7] F. Hilario, V. Roche, R.P. Nogueira, A.M.J. Junior, Influence of morphology and crystalline structure of $TiO_2$ nanotubes on their electrochemical properties and apatite-forming ability, Electrochim. Acta. 245 (2017) 337–349. https://doi.org/10.1016/j.electacta.2017.05.160.

[8] Y. Wang, C. Wen, P. Hodgson, Y. Li, Biocompatibility of $TiO_2$ nanotubes with different topographies, J. Biomed. Mater. Res. - Part A. 102 (2014) 743–751. https://doi.org/10.1002/jbm.a.34738.

[9] S. Minagar, C.C. Berndt, J. Wang, E. Ivanova, C. Wen, A review of the application of anodization for the fabrication of nanotubes on metal implant surfaces, Acta Biomater. 8 (2012) 2875–2888. https://doi.org/10.1016/j.actbio.2012.04.005.

[10] N.K. Awad, S.L. Edwards, Y.S. Morsi, A review of $TiO_2$ NTs on Ti metal: Electrochemical synthesis, functionalization and potential use as bone implants, Mater. Sci. Eng. C. 76 (2017) 1401–1412. https://doi.org/10.1016/j.msec.2017.02.150.

[11] R.J. Narayan, ASM Handbook, Volume 23 Materials for Medical Devices, 1 st, 2012.

[12] S. Noumbissi, A. Scarano, S. Gupta, A literature review study on atomic ions dissolution of titanium and its alloys in implant dentistry, Materials (Basel). 12 (2019) 1–15. https://doi.org/10.3390/ma12030368.

[13] D.M. Gordin, R. Ion, C. Vasilescu, S.I. Drob, A. Cimpean, T. Gloriant, Potentiality of the “gum Metal” titanium-based alloy for biomedical applications, Mater. Sci. Eng. C. 44 (2014) 362–370. https://doi.org/10.1016/j.msec.2014.08.003.

[14] M.F. Ijaz, C. Vasilescu, S.I. Drob, P. Osiceanu, M. Marcu, H.Y. Kim, S. Miyazaki, D.M. Gordin, T. Gloriant, Electrochemical characterization of the superelastic (Ti-Zr)-Mo-Sn biomedical alloy displaying a large recovery strain, Mater. Corros. 68 (2017) 1220–1227. https://doi.org/10.1002/maco.201709484.

[15] E. Vasilescu, P. Drob, D. Raducanu, I. Cinca, D. Mareci, J.M. Calderon Moreno, M. Popa, C. Vasilescu, J.C. Mirza Rosca, Effect of thermo-mechanical processing on the corrosion resistance of Ti6Al4V alloys in biofluids, Corros. Sci. 51 (2009) 2885–2896. https://doi.org/10.1016/j.corsci.2009.08.014.

[16] M.L.D.C.R.D.A. Carvalho, Corrosion of copper alloys in natural seawater – Effects of hydrodynamics and pH, Université Pierre et Marie Curie, 2014.

[17] M. Itagaki, S. Suzuki, I. Shitanda, K. Watanabe, H. Nakazawa, Impedance analysis on electric double layer capacitor with transmission line model, J. Power Sources. 164 (2007) 415–424. https://doi.org/10.1016/j.jpowsour.2006.09.077.

[18] F. Hilario, V. Roche, A.M. Jorge, R.P. Nogueira, Application of the transmission line model for porous electrodes to analyse the impedance

response of $TiO_2$ nanotubes in physiological environment, Electrochim. Acta. 253 (2017) 599–608. https://doi.org/10.1016/j.electacta.2017.09.045.

[19] C. Martínez, C. Guerra, D. Silva, M. Cubillos, F. Briones, L. Muñoz, M.A. Páez, C. Aguilar, M. Sancy, Effect of porosity on mechanical and electrochemical properties of Ti–6Al–4V alloy, Electrochim. Acta. 338 (2020) 2–11. https://doi.org/10.1016/j.electacta.2020.135858.

[20] C. Guerra, M. Sancy, M. Walczak, D. Silva, C. Martínez, B. Tribollet, C. Aguilar, Evolution of oxide film on the internal porosity of Ti-30Nb-13Ta-2Mn alloy foam, Electrochim. Acta. 283 (2018) 676–682. https://doi.org/10.1016/j.electacta.2018.05.010.

[21] S. Fletcher*, The two-terminal equivalent network of a three-terminal electrochemical cell, Electrochim. Acta. 55 (2010) 1907–1911. https://doi.org/10.1016/j.electacta.2009.11.008.

[22] F. HILARIO, Synthèse et caractérisations de nanotubes de $TiO_2$ pour applications biomédicales : propriétés électrochimiques et bioactivité, Université Grenoble Alpes, 2018.

[23] B.E. Torres Bautista, M.L. Carvalho, A. Seyeux, S. Zanna, P. Cristiani, B. Tribollet, P. Marcus, I. Frateur, Effect of protein adsorption on the corrosion behavior of 70Cu-30Ni alloy in artificial seawater, Bioelectrochemistry. 97 (2014) 34–42. https://doi.org/10.1016/j.bioelechem.2013.10.004.

[24] NIST X-ray Photoelectron Spectroscopy Database, NIST Standard Reference Database Number 20, National Institute of Standards and Technology,

Gaithersburg MD, 20899 (2000), (n.d.). https://doi.org/10.18434/T4T88K.

[25] L.L. Marciniuk, P. Hammer, H.O. Pastore, U. Schuchardt, D. Cardoso, Sodium titanate as basic catalyst in transesterification reactions, Fuel. 118 (2014) 48–54. https://doi.org/10.1016/j.fuel.2013.10.036.

[26] J.E. Berger, A.M. Jorge Jr, G.H. Asato, V. Roche, Formation of self-ordered oxide nanotubes layer on the equiatomic TiNbZrHfTa high entropy alloy and bioactivation procedure, J. Alloys Compd. 865 (2021) 158837. https://doi.org/10.1016/j.jallcom.2003.09.093.

[27] B.R. Anwar M., Hogarth C.A., se ( ICSD ) SRD 3 . For more information visit https://ic, J. Mater. Sci. 24 (1989) 3087.

[28] J.L. Xu, S.C. Tao, L.Z. Bao, J.M. Luo, Y.F. Zheng, Effects of Mo contents on the microstructure, properties and cytocompatibility of the microwave sintered porous Ti-Mo alloys, Mater. Sci. Eng. C. 97 (2019) 156–165. https://doi.org/10.1016/j.msec.2018.12.028.

[29] Y.L. Zhou, D.M. Luo, Corrosion behavior of Ti-Mo alloys cold rolled and heat treated, J. Alloys Compd. 509 (2011) 6267–6272. https://doi.org/10.1016/j.jallcom.2011.03.045.

[30] A.K. Shukla, R. Balasubramaniam, S. Bhargava, Properties of passive film formed on CP titanium, Ti-6Al-4V and Ti-13.4Al-29Nb alloys in simulated human body conditions, Intermetallics. 13 (2005) 631–637. https://doi.org/10.1016/j.intermet.2004.10.001.

[31] S.Y. Kim, Y.K. Kim, Y.S. Jang, I.S. Park, S.J. Lee, J.G. Jeon, M.H. Lee,

Bioactive effect of alkali-heat treated $TiO_2$ nanotubes by water or acid treatment, Surf. Coatings Technol. 303 (2016) 256–267. https://doi.org/10.1016/j.surfcoat.2016.03.074.

[32] S. Tamilselvi, V. Raman, N. Rajendran, Surface modification of titanium by chemical and thermal methods - Electrochemical impedance spectroscopic studies, Corros. Eng. Sci. Technol. 46 (2011) 585–591. https://doi.org/10.1179/147842209X12590591256936.

[33] V. Augustyn, P. Simon, B. Dunn, Pseudocapacitive oxide materials for high-rate electrochemical energy storage, Energy Environ. Sci. 7 (2014) 1597–1614. https://doi.org/10.1039/c3ee44164d.

[34] M.E. Orazem, N. Pȁbre, B. Tribollet, Enhanced graphical representation of electrochemical impedance data, J. Electrochem. Soc. 153 (2006) 129–136. https://doi.org/10.1149/1.2168377.

[35] H. Liu, J. Yang, X. Zhao, Y. Sheng, W. Li, C.L. Chang, Q. Zhang, Z. Yu, X. Wang, Microstructure, mechanical properties and corrosion behaviors of biomedical Ti-Zr-Mo-xMn alloys for dental application, Corros. Sci. 161 (2019) 2–15. https://doi.org/10.1016/j.corsci.2019.108195.

[36] P. Córdoba-Torres, N.T.C. Oliveira, C. Bolfarini, V. Roche, R.P. Nogueira, Electrochemical impedance analysis of $TiO_2$ nanotube porous layers based on an alternative representation of impedance data, J. Electroanal. Chem. 737 (2015) 54–64. https://doi.org/10.1016/j.jelechem.2014.06.034.

[37] Mark E. Orazem, B. Tribollett, Electrochemical Impedance Spectroscopy, in:

Agric. Food Electroanal., Second edi, 2015: pp. 381–419. https://doi.org/10.1002/9781118684030.ch14.

[38] S.L. De Assis, S. Wolynec, I. Costa, Corrosion characterization of titanium alloys by electrochemical techniques, Electrochim. Acta. 51 (2006) 1815–1819. https://doi.org/10.1016/j.electacta.2005.02.121.

[39] D.Q. Martins, W.R. Osório, M.E.P. Souza, R. Caram, A. Garcia, Effects of Zr content on microstructure and corrosion resistance of Ti-30Nb-Zr casting alloys for biomedical applications, Electrochim. Acta. 53 (2008) 2809–2817. https://doi.org/10.1016/j.electacta.2007.10.060.

[40] A. Kocijan, D.K. Merl, M. Jenko, The corrosion behaviour of austenitic and duplex stainless steels in artificial saliva with the addition of fluoride, Corros. Sci. 53 (2011) 776–783. https://doi.org/10.1016/j.corsci.2010.11.010.

[41] K.B. Devi, K. Singh, N. Rajendran, Synthesis and characterization of nanoporous sodium-substituted hydrophilic titania ceramics coated on 316L SS for biomedical applications, J. Coatings Technol. Res. 8 (2011) 595–604. https://doi.org/10.1007/s11998-011-9344-z.

[42] S. Gudi, J. Radoševi, M. Kliški, Study of passivation of Al and Al-Sn alloys in borate buffer solutions using electrochemical impedance spectroscopy, Electrochim. Acta. 47 (2002) 3009–3016. https://doi.org/10.1016/S0013-4686(02)00246-3.

[43] T. Kokubo, F. Miyaji, H.-M. Kim, T. Nakamura, Spontaneous Formation of Bonelike Apatite Layer on Chemically Treated Titanium Metals, J. Am. Ceram.

Soc. 79 (1996) 1127–1129. https://doi.org/10.1111/j.1151-2916.1996.tb08561.x.

[44] H.M. Kim, F. Miyaji, T. Kokubo, T. Nakamura, Preparation of bioactive Ti and its alloys via simple chemical surface treatment., J. Biomed. Mater. Res. 32 (1996) 409–417. https://doi.org/10.1002/(SICI)1097-4636(199611)32:3<409::AID-JBM14>3.0.CO;2-B.

[45] L. Jonásová, F. a Müller, A. Helebrant, J. Strnad, P. Greil, Hydroxyapatite formation on alkali-treated titanium with different content of Na+ in the surface layer., Biomaterials. 23 (2002) 3095–101. http://www.ncbi.nlm.nih.gov/pubmed/12102180.

[46] L. Jonášová, F. a. Müller, A. Helebrant, J. Strnad, P. Greil, Biomimetic apatite formation on chemically treated titanium, Biomaterials. 25 (2004) 1187–1194. https://doi.org/10.1016/j.biomaterials.2003.08.009.

[47] S. Ban, Y. Iwaya, H. Kono, H. Sato, Surface modification of titanium by etching in concentrated sulfuric acid, Dent. Mater. 22 (2006) 1115–1120. https://doi.org/10.1016/j.dental.2005.09.007.

[48] R. de Levie, On porous electrodes in electrolyte solutions*, Electrochim. Acta. 9 (1964) 1231–1245. https://doi.org/10.1016/0013-4686(64)85015-5.

[49] J. Bisquert, Influence of the boundaries in the impedance of porous film electrodes, Phys. Chem. Chem. Phys. 2 (2000) 4185–4192. https://doi.org/10.1039/b001708f.

[50] G. Garcia-Belmonte, J. Bisquert, E.C. Pereira, F. Fabregat-Santiago,

Switching behaviour in lightly doped polymeric porous film electrodes. Improving distributed impedance models for mixed conduction conditions, J. Electroanal. Chem. 508 (2001) 48–58. https://doi.org/10.1016/S0022-0728(01)00504-6.

[51] C. Shuai, H. Sun, P. Wu, C. Gao, Y. Yang, W. Guo, D. Yang, F. Xu, P. Feng, S. Peng, Biosilicate scaffolds for bone regeneration: Influence of introducing SrO, RSC Adv. 7 (2017) 21749–21757. https://doi.org/10.1039/c7ra01606a.

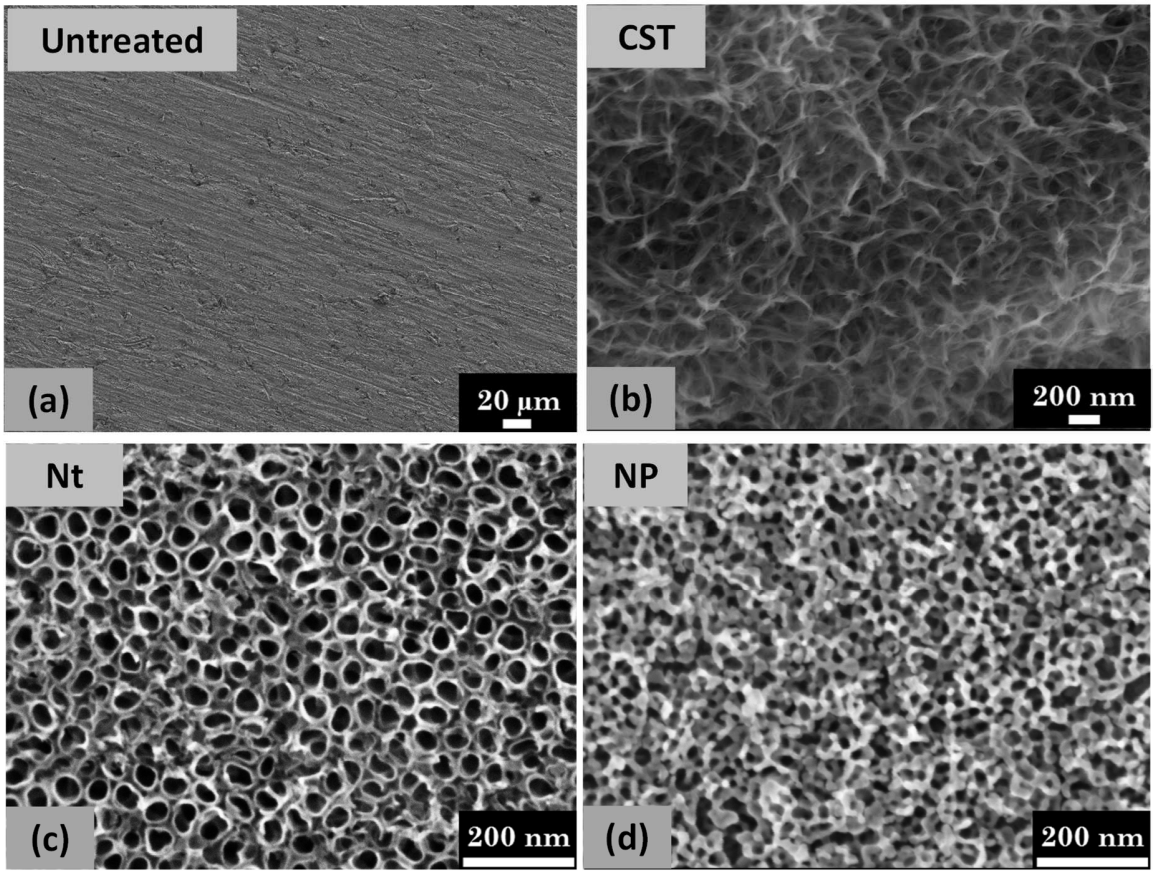


Fig. 1. SEM image of TMZF alloy: a) Untreated after polishing and grinding, b) chemically treated by HCl 37% at 60 °C and NaOH 10 mol·L$^{-1}$ at 60 °C for 24 h, c) and d) anodised with Nt and NP, respectively.

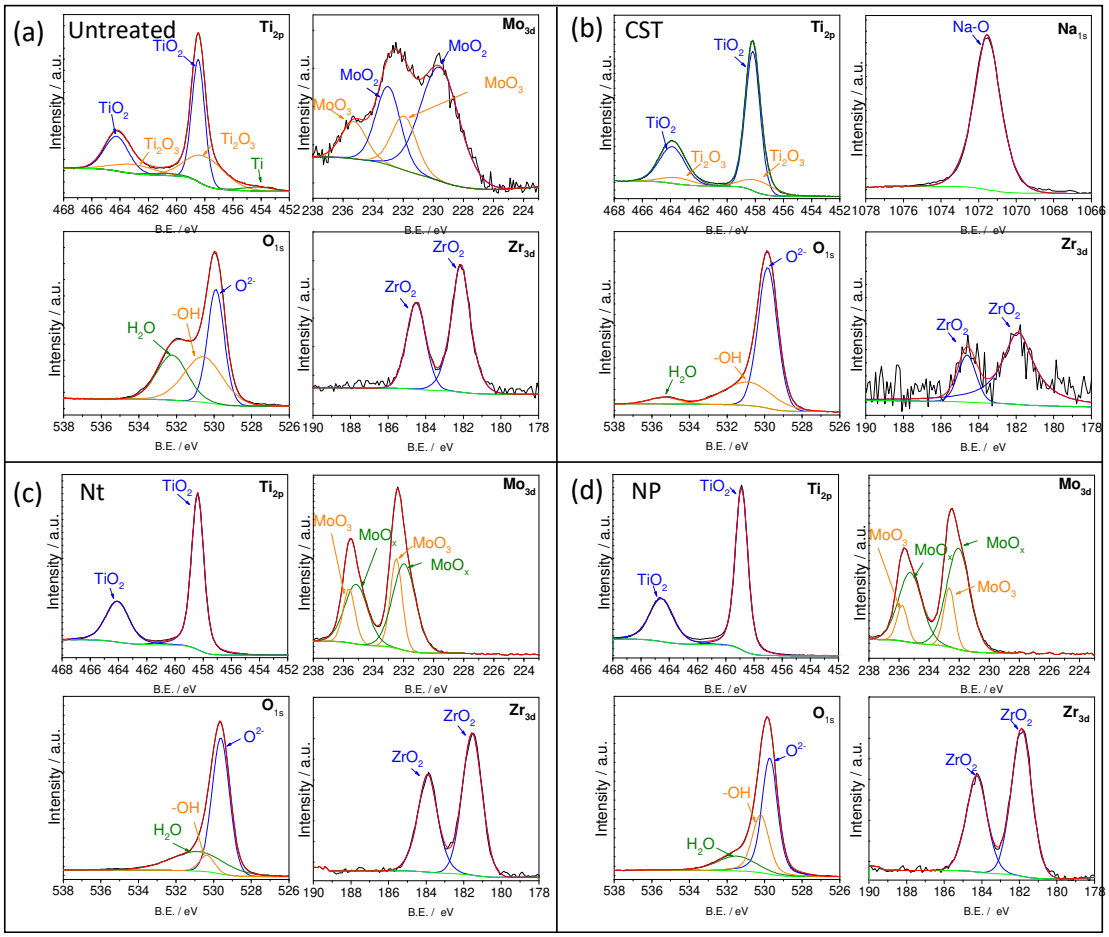


Fig. 2 High-resolution XPS spectra of Ti2p, Mo3d, O1s, Zr3d, and Na 1s obtained for the different surface condition: a) Untreated; b) CST; c) Nt and d) NP.

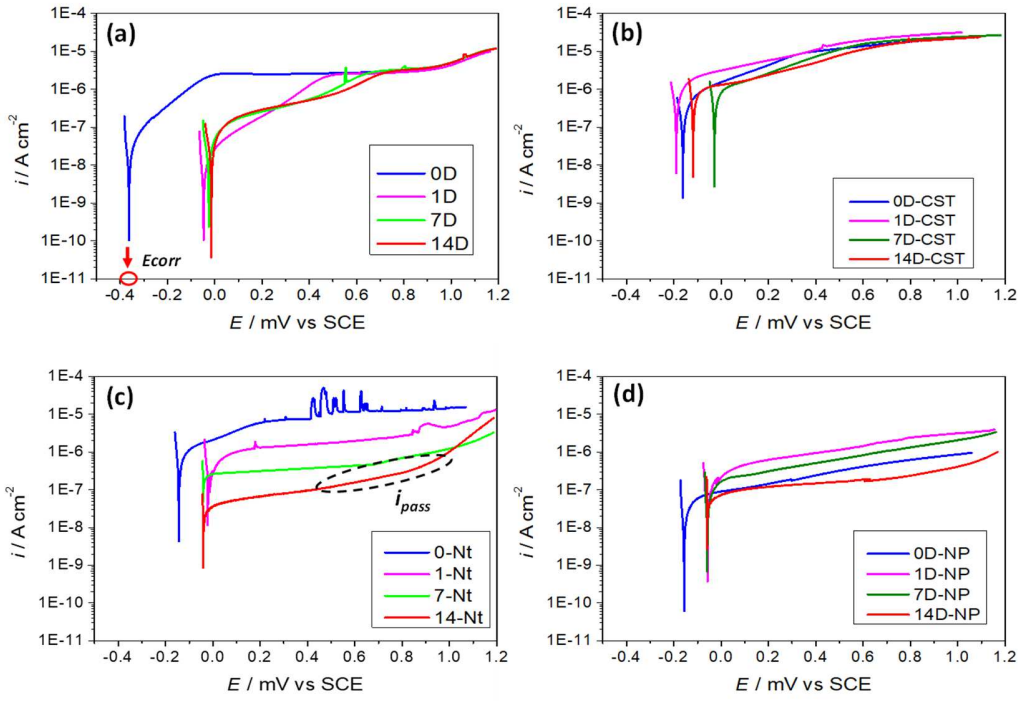


Fig. 3. Anodic polarization curves for the TMZF alloy in SBF electrolyte at 37 °C: a) Untreated; b) CST; c) Nt and d) NP.

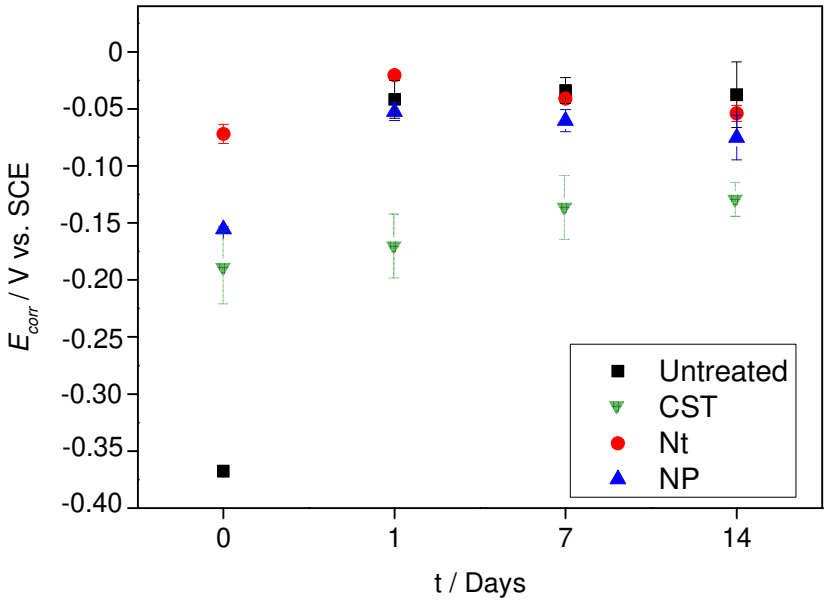


Fig. 4. Electrochemical measurements of corrosion potential ($E_{corr}$) of TMZF alloy untreated and treated with Nt, NP, and CST for different immersion times in SBF at 37°C (the error bars were obtained from the standard deviation results of three samples per condition and soaking time).

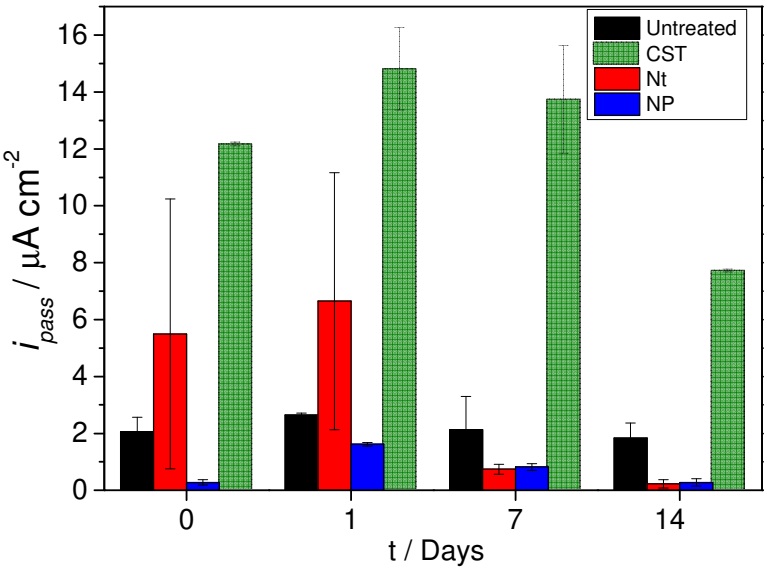


Fig 5. Electrochemical measurements of passivation current density ($i_{pass}$) of TMZF alloy untreated and treated with Nt, NP, and CST in different immersion times in SBF at 37°C (the error bars were obtained from the standard deviation results of three tested samples per condition and soaking time).

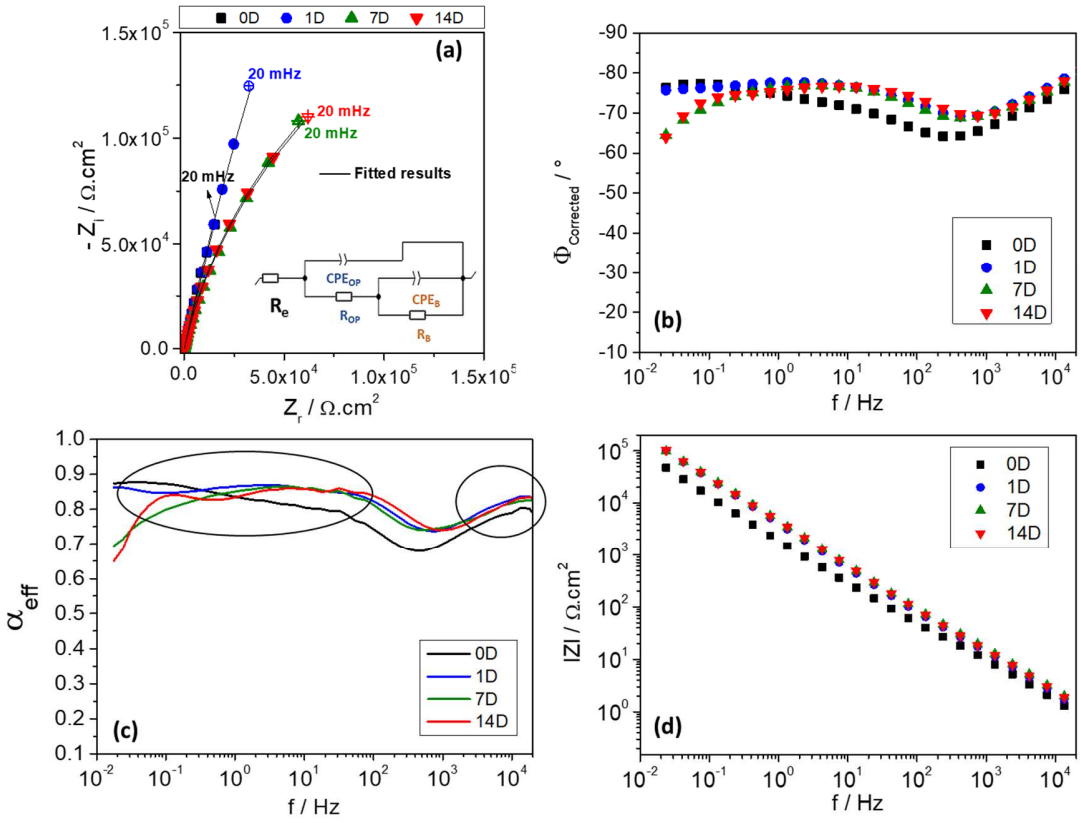


Fig. 6. Impedance results for untreated samples immersed in SBF at 37 °C for the different immersion time (0, 1, 7, and 14 days denoted as 0D, 1D, 7D, and 14D respectively): a) Nyquist plots of experimental and simulated results obtained using SIMAD software and the electrical equivalent circuit employed; b) Corrected-phase angle; c) Evolution of $\alpha_{eff}$ versus frequency and d) Corrected-Modulus of the impedance.

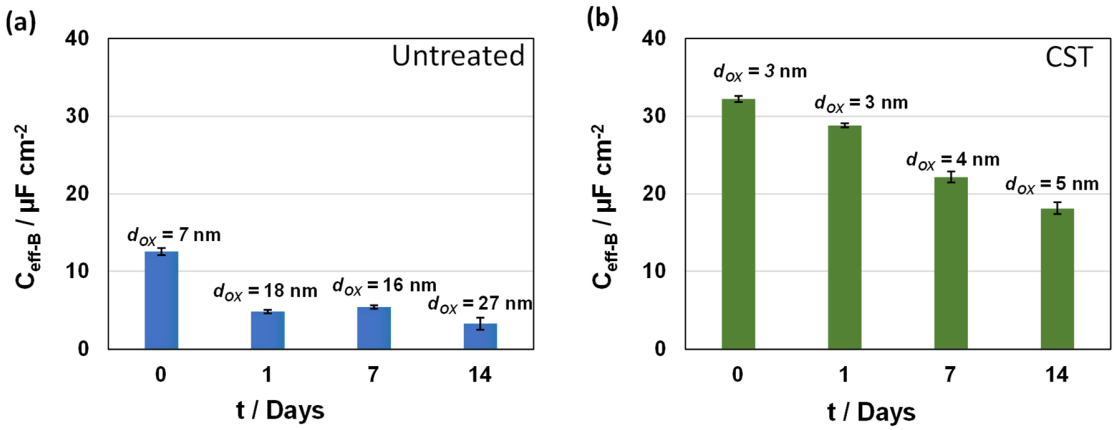


Fig. 7. Effective capacitances and thickness evolution of the passive inner layer during different immersion days in SBF solution at 37 °C: a) Untreated and b) CST. (these values were calculated from Tables 1 and 2).

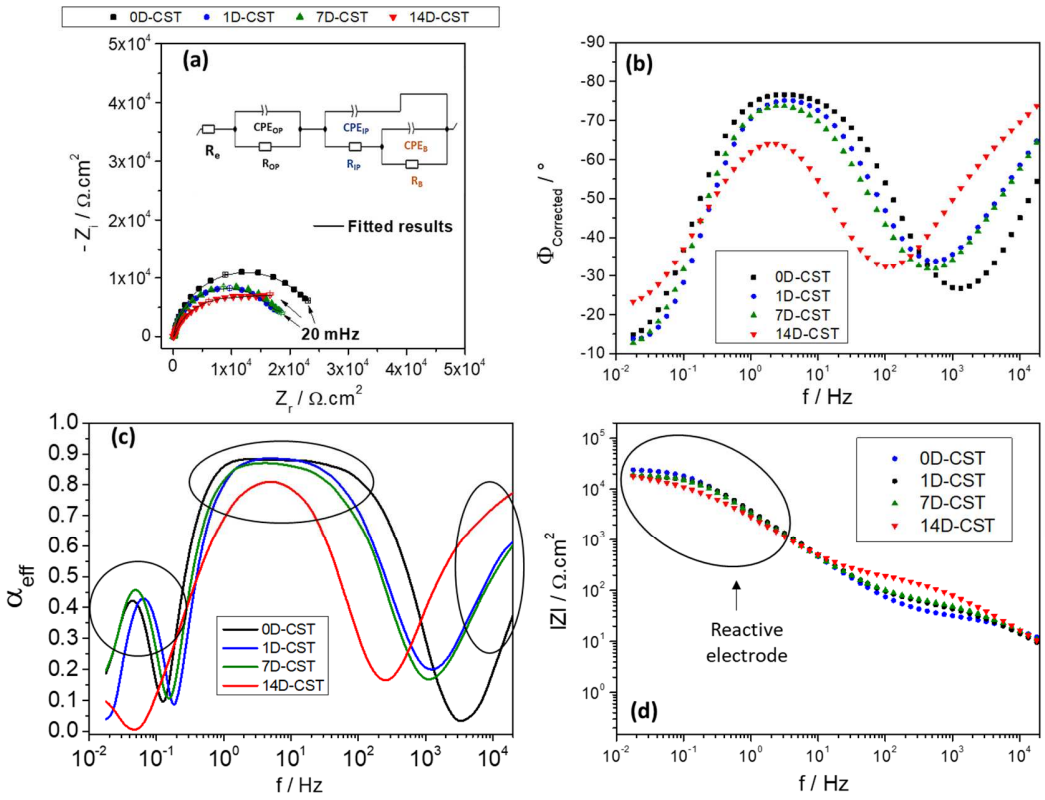


Fig. 8. Impedance results for CST samples immersed in SBF at 37 °C for the different immersion times (0, 1, 7, and 14 days denoted as 0D, 1D, 7D, and 14D respectively): a) Nyquist plots of experimental and simulated results obtained through the SIMAD software and the electrical equivalent circuit employed; b) Corrected-phase angle; c) Evolution of $\alpha_{eff}$ versus frequency and d) Corrected-Modulus of the impedance.

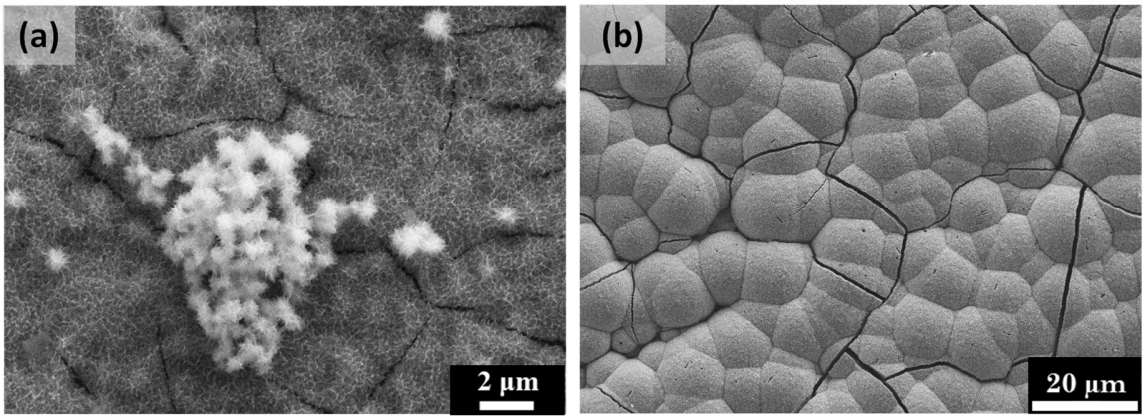


Fig. 9. SEM images for CST samples after different immersion periods in SBF: a) 7 days, showing some nucleus of calcium phosphate on the sample surface, and b) 14 days.

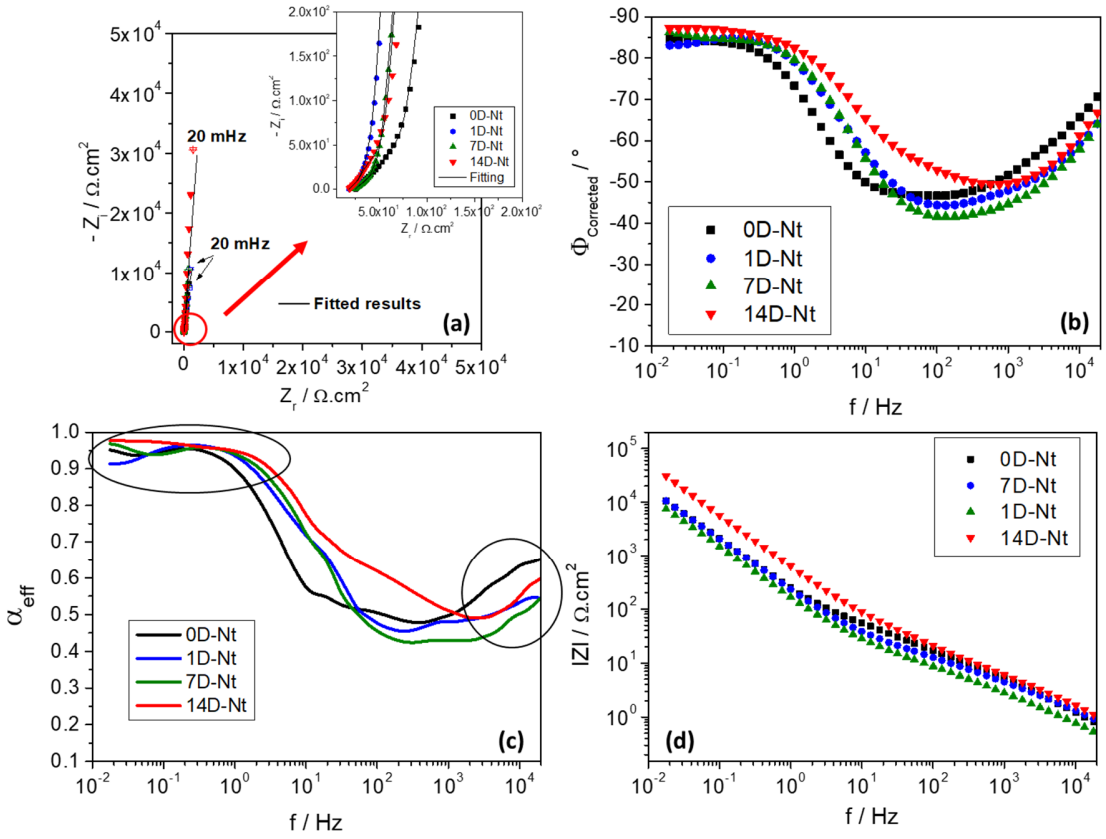


Fig. 10. Impedance results for Nt samples immersed in SBF at 37 °C for the different immersion time (0, 1, 7, and 14 days denoted as 0D, 1D, 7D, and 14D respectively): a) Nyquist plots of experimental and simulated results obtained using SIMAD software and the electrical equivalent circuit employed; b) Corrected-phase angle; c) Evolution of $\alpha_{eff}$ versus frequency and d) Corrected-Modulus of the impedance.

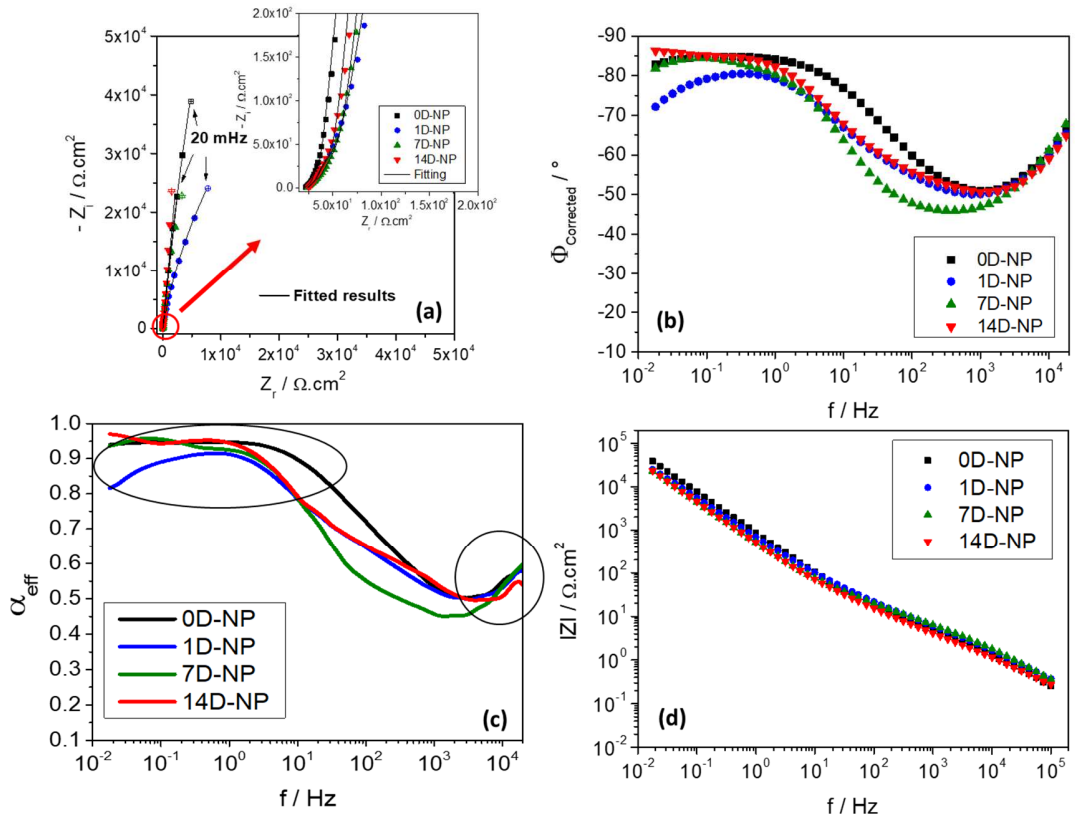


Fig. 11. Impedance results for NP samples immersed in SBF at 37 °C for the different immersion time (0, 1, 7, and 14 days denoted as 0D, 1D, 7D, and 14D respectively): a) Nyquist plots of experimental and simulated results obtained using SIMAD software and the electrical equivalent circuit employed; b) Corrected-phase angle; c) Evolution of $\alpha_{eff}$ versus frequency and d) Corrected-Modulus of the impedance.

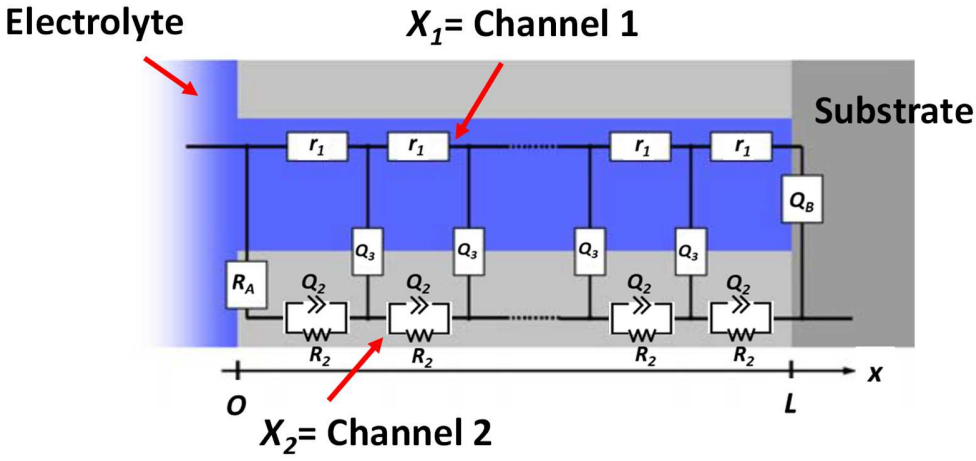


Fig. 12. The transmission line model proposed to describe the impedance response of the anodised TMZF samples immersed in SBF at 37 °C during the different periods evaluated.

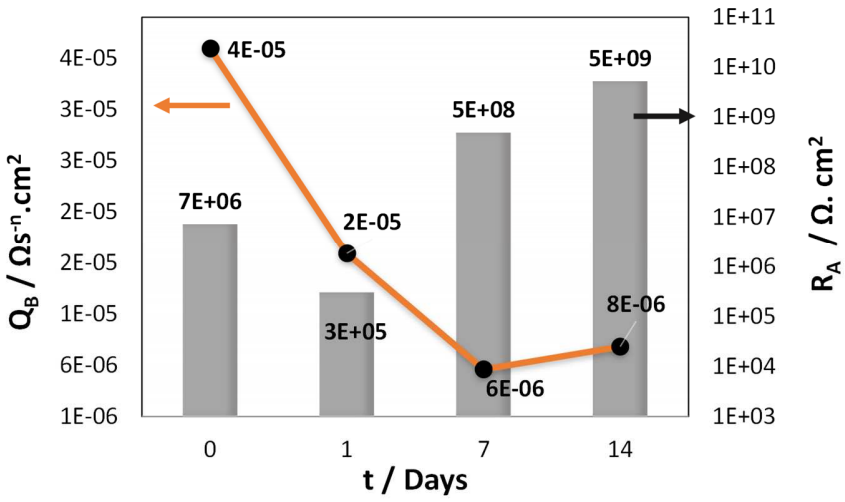


Fig. 13. Endpoints parameters, $R_A$ and $Q_B$, were obtained from the transmission line model used in nanotubes samples after different immersion periods in SBF.

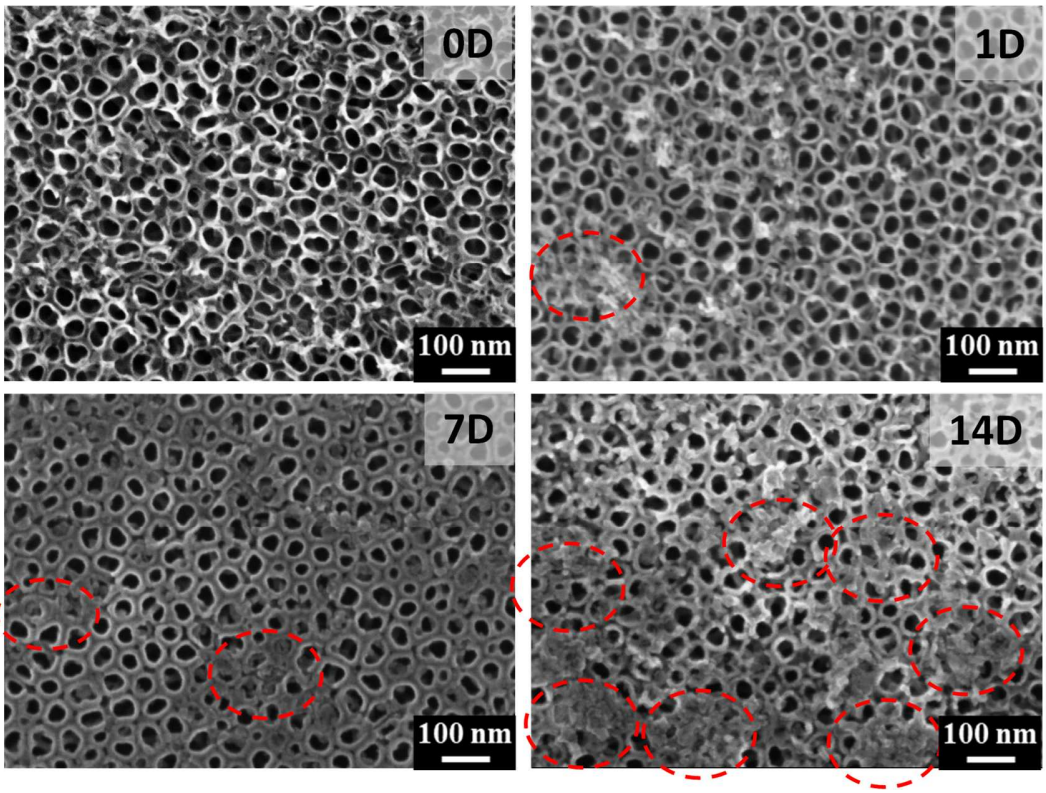


Fig. 14. Apatite formation over Nt samples after different immersion periods in SBF (0, 1, 7, and 14 days).

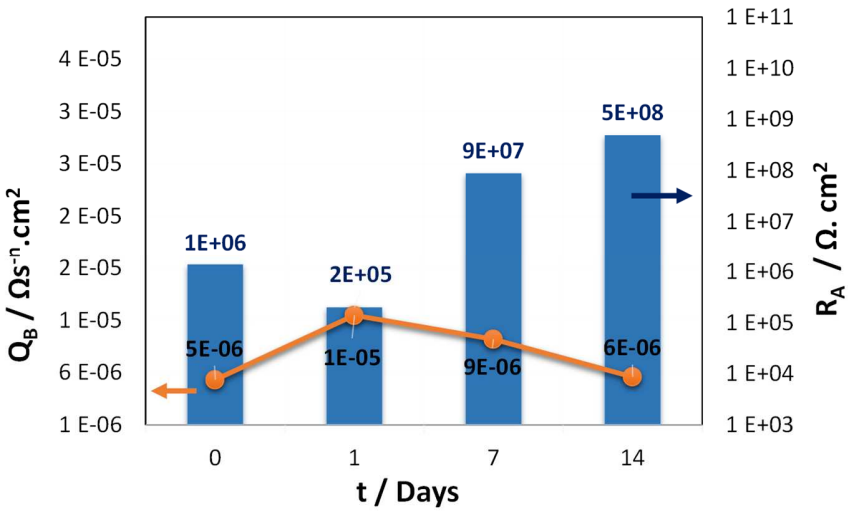


Fig. 15. Endpoints parameters, $R_A$ and $Q_B$, obtained from the transmission line model used in NP samples after different immersion periods in SBF.

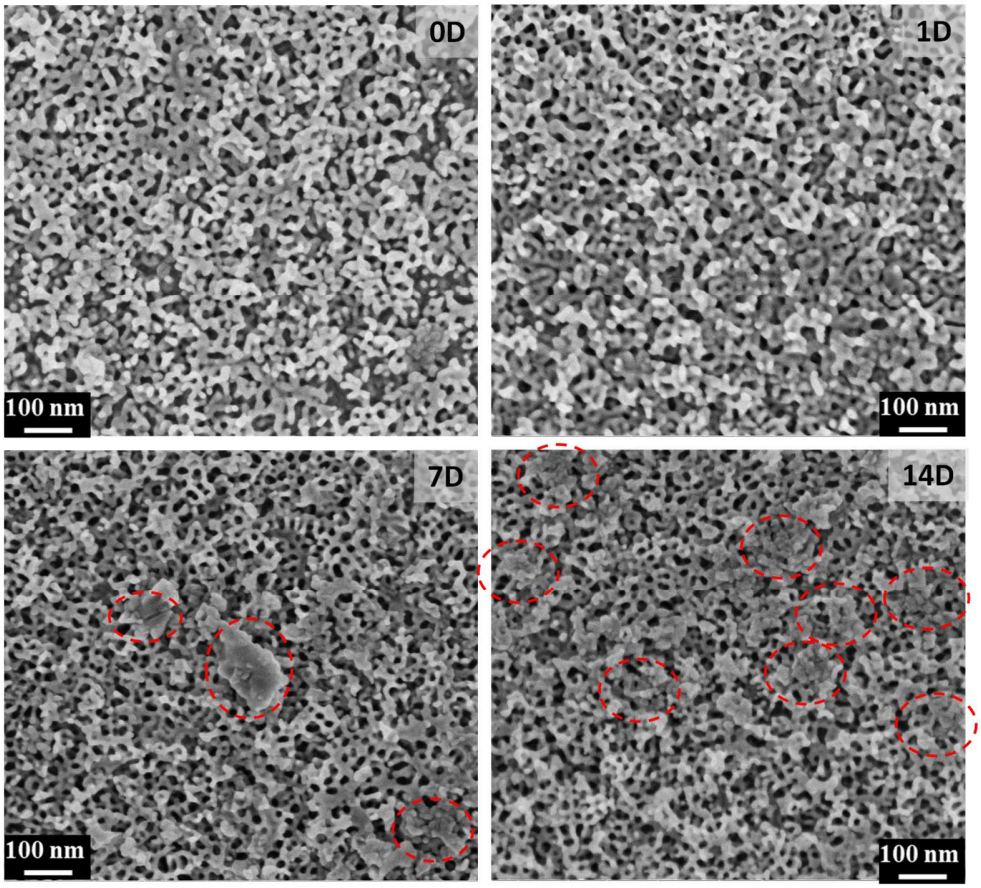


Fig. 16. Apatite formation over NP samples after different immersion periods in SBF (0, 1, 7, and 14 days).

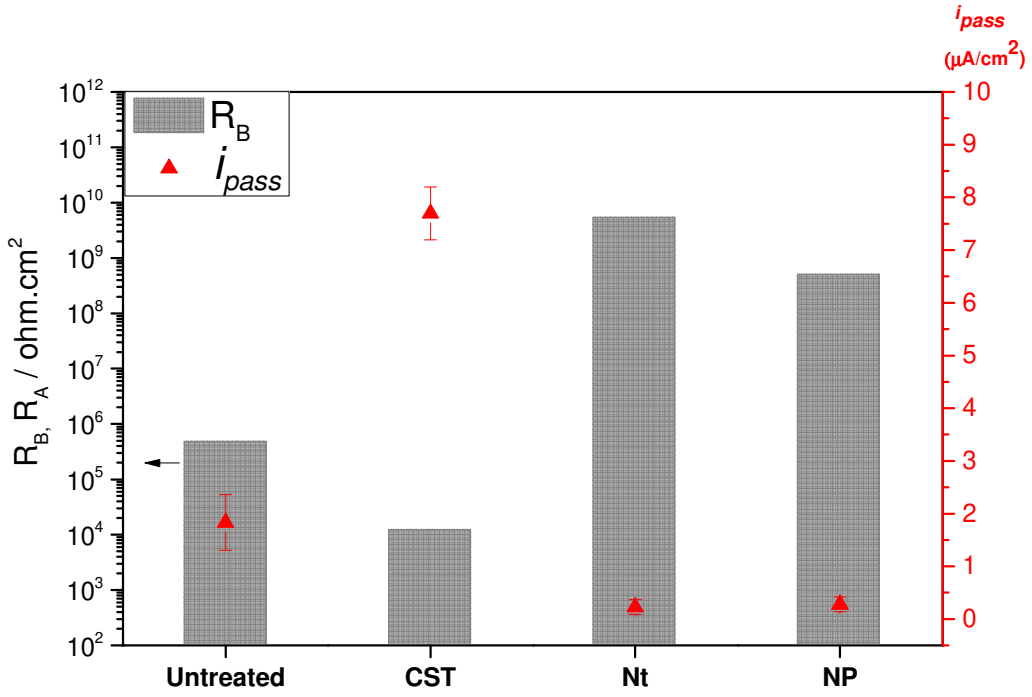


Fig. 17. Corrosion response of untreated CST, Nt, and NP samples after 14 days of immersion in SBF at 37 °C. Barrier resistance ($R_B$ or $R_A$ for the anodised samples) obtained from the impedance data, and passivation current ($i_{pass}$) from the polarization curves.

Table 1 Electrical parameters of the equivalent circuit obtained by fitting the experimental results of impedance for untreated samples at 37 °C in the SBF solution.

| Immersion Days | $R_e$ ($\Omega$-cm$^2$) | $Q_{OP}$ ($\Omega s^{-\alpha}.cm^2$) | $\alpha_{OP}$ | $R_{OP}$ ($\Omega$-cm$^2$) | $Q_B$ ($\Omega s^{-\alpha}.cm^2$) | $\alpha_B$ | $R_B$ ($10^5\Omega$-cm$^2$) | $X$ (%) |
|---|---|---|---|---|---|---|---|---|
| 0 | 23 | 1.74E-05 | 0.85 | 94 | 1.37E-05 | 0.83 | 2.83 | 0.45 |
| 1 | 20 | 8.35E-06 | 0.88 | 63 | 6.02E-06 | 0.84 | 2.90 | 0.23 |
| 7 | 21 | 4.80E-06 | 0.92 | 49 | 8.55E-06 | 0.81 | 4.64 | 0.22 |
| 14 | 20 | 1.04E-05 | 0.84 | 77 | 2.95E-06 | 0.88 | 4.60 | 0.77 |

Table 2 Electrical impedance parameters obtained by fitting the experimental results of CST samples immersed in SBF at 37 °C for the different periods 0, 1, 7, and 14 days.

| Immersion Days | $R_e$ ($\Omega$.cm$^2$) | $Q_{OP}$ ($\Omega s^{-\alpha}.cm^2$) | $\alpha_{OP}$ | $R_{OP}$ ($\Omega$.cm$^2$) | $Q_{IP}$ ($\Omega s^{-\alpha}.cm^2$) | $\alpha_{IP}$ | $R_{IP}$ ($\Omega$.cm$^2$) | $Q_B$ ($\Omega s^{-\alpha}.cm^2$) | $\alpha_B$ | $R_B$ ($\Omega$.cm$^2$) | $C_{effB}$ ($\mu$F/cm$^2$) | $X$ (%) |
|---|---|---|---|---|---|---|---|---|---|---|---|---|
| 0 | 25 | 8.61 E-04 | 0.57 | 35.05 | 3.31 E-06 | 0.71 | 819 | 1.69 E-05 | 0.91 | 48562 | 32 | 0.39 |
| 1 | 21 | 2.79 E-04 | 0.55 | 50.14 | 6.66 E-06 | 0.72 | 283 | 1.39 E-05 | 0.95 | 16366 | 29 | 0.26 |
| 7 | 24 | 3.30 E-04 | 0.53 | 112.33 | 9.28 E-06 | 0.60 | 283 | 2.46 E-05 | 0.84 | 11916 | 22 | 0.71 |
| 14 | 23 | 1.45 E-04 | 0.80 | 178.97 | 4.08 E-06 | 0.76 | 155 | 1.81 E-05 | 0.85 | 11513 | 18 | 0.82 |

Table 3 Electrical impedance parameters obtained by adjusting the experimental results of Nt samples.

| Days | X1 | | X2 | | ζ | | $Z_A$ | $Z_B$ | | L | ωc | *X* |
|---|---|---|---|---|---|---|---|---|---|---|---|---|
| | $R_1$ (Ω.cm) | $R_2$ (Ω.cm²) | $Q_2$ (Ωs$^{-e}$.cm²) | e | $Q_3$ (Ωs$^{-b}$.cm) | b | $R_A$ (Ω.cm²) | $Q_B$ (Ωs$^{-n}$.cm²) | n | (cm) | (Hz) | (%) |
| 0 | 827 | 217 | 6.53 E-07 | 0.96 | 1.63 E-04 | 0.96 | 7.22 E+06 | 3.69 E-05 | 0.91 | 2.0 E-05 | 0.035 | 0.77 |
| 1 | 956 | 222 | 4.55 E-07 | 0.76 | 2.96 E-04 | 0.96 | 2.99 E+05 | 1.69 E-05 | 0.84 | 2.0 E-05 | 0.023 | 0.48 |
| 7 | 938 | 209 | 6.06 E-07 | 0.78 | 3.91 E-04 | 0.95 | 4.90 E+08 | 5.58 E-06 | 0.92 | 2.0 E-05 | 0.019 | 0.43 |
| 14 | 860 | 145 | 2.81 E-06 | 0.72 | 9.96 E-05 | 0.96 | 5.25 E+09 | 7.80 E-06 | 0.89 | 2.0 E-05 | 0.003 | 1.70 |

Table 4 Electrical impedance parameters obtained by adjusting the experimental results of NP samples.

| Days | X1 | | X2 | | ζ | | $Z_A$ | $Z_B$ | | L | ωc | *X* |
|---|---|---|---|---|---|---|---|---|---|---|---|---|
| | $R_1$ (Ω.cm) | $R_2$ (Ω.cm²) | $Q_2$ (Ωs$^{-e}$.cm²) | e | $Q_3$ (Ωs$^{-b}$.cm) | b | $R_A$ (Ω.cm²) | $Q_B$ (Ωs$^{-n}$.cm²) | n | (cm) | (Hz) | (%) |
| **0** | 559 | 203 | 8.52 E-07 | 0.60 | 7.73 E-05 | 0.96 | 1.40 E+06 | 5.32 E-06 | 0.90 | 2.0E-05 | 0.003 | 0.60 |
| **1** | 826 | 207 | 9.24 E-07 | 0.64 | 7.52 E-05 | 0.97 | 2.00 E+05 | 1.15.E-05 | 0 82 | 2.0E-05 | 0.004 | 0.97 |
| **7** | 787 | 209 | 6.06 E-07 | 0.96 | 8.68 E-05 | 0.97 | 8.83 E+07 | 9.18 E-06 | 0.92 | 2.0E-05 | 0.004 | 0.43 |
| **14** | 936 | 218 | 6.88 E-07 | 0.60 | 7.60 E-05 | 0.97 | 4.90 E+08 | 5.59 E-06 | 0.89 | 2.0E-05 | 0.003 | 1.00 |